Materials Horizons

Post-Assembly Dimension-Dependent Face-Selective Etching of Fullerene Crystals

Journal:	*Materials Horizons*
Manuscript ID	MH-COM-11-2019-001866.R1
Article Type:	Communication
Date Submitted by the Author:	29-Nov-2019

Complete List of Authors:	Hsieh, Cheng-Tien; National Taiwan University, Institute of Polymer Science and Engineering Hsu, Shan-hui; National Taiwan University, Polymer Science and Engineering Chahal, Mandeep K.; National Institute for Materials Science, International Center for Materials Nanoarchitectonics Maji, Subrata; National Institute for Materials Science (NIMS), WPI Center for Materials Nanoarchitectonics (MANA) Song, Jingwen ; The University of Tokyo Graduate School of Frontier Sciences Hill, Jonathan; National Institute for Materials Science, International Center for Materials Nanoarchitectonics Ariga, Katsuhiko; National Institute for Materials Science, World Premier International (WPI) Research Center for Materials Nanoarchitectonics (MANA) Shrestha, Lok Kumar; National Institute for Materials Science (NIMS), WPI Center for Materials Nanoarchitectonics (MANA)

ARTICLE

Post-Assembly Dimension-Dependent Face-Selective Etching of Fullerene Crystals

Received 00th January 20xx,
Accepted 00th January 20xx

DOI: 10.1039/x0xx00000x

Cheng-Tien Hsieh,[a] Shan-hui Hsu,*[a] Mandeep Chahal,[b] Subrata Maji,[b] Jingwen Song,[c] Jonathan P. Hill,[b] Katsuhiko Ariga,*[bc] Lok Kumar Shrestha*[b]

Here we report the face-selective chemical etching of fullerene crystals in solvent under ambient conditions of temperature and pressure. First, fullerene C_{60} nanorods (FNR), fullerene C_{60} nanosheet (FNS) and fullerene C_{70} cubes (FC) were prepared using ultrasound assisted liquid-liquid interfacial precipitation (ULLIP). Chemical etching of these crystals was then performed using ethylene diamine (EDA), which results in selective etching at the ends of FNRs forming hollow-structured fullerene nanotubes. For two dimensional FNS, etching occurs mostly at the upper and lower surfaces of the sheets with partial etching at the edges. For three dimensional FCs, etching occurs on all faces of the cubes leading to the formation of object with gyroid-like morphology. In addition to the excellent water dispersibility due to EDA functionalization, chemically etched fullerene nanostructures showed excellent vapor sensing performance selective for acid vapors (formic or acetic acids) over aromatic vapors (benzene or toluene). In contrast to the established yet costly lithography techniques used to make microstructures, this is a simple and scalable solution process, and it presents a low-cost strategy for which we have coined the term 'beaker lithography' for the construction of hollow fullerene nanostructures.

New concepts

Here we report the first example of the face-selective chemical etching of fullerene crystals in solvent under ambient conditions of temperature and pressure. Fullerene C_{60} nanorods, fullerene C_{60} nanosheet and fullerene C_{70} cubes were prepared using the ultrasound assisted liquid-liquid interfacial precipitation. Chemical etching of these crystals was then performed using ethylenediamine resulting in selective etching at the ends of fullerene nanorods and the formation of hollow-structured fullerene nanotubes. For two dimensional fullerene nanosheets, etching occurs mostly at the upper and lower surfaces of the sheets with partial etching at the edges. For three dimensional fullerene cubes, etching occurs on all faces of the cubes leading to the formation of objects with gyroid-like morphology. In addition to the excellent water dispersibility, chemically etched fullerene nanostructures showed excellent vapor sensing performance selective for acid vapors (formic or acetic acids) over aromatic vapors (benzene or toluene). In contrast to the established yet costly lithographic techniques used to fabricate microstructures,

Introduction

The recently developed concept of nanoarchitectonics has enabled atomic and molecular level manipulation for the arrangement of nanoscale structural units or building blocks in a specific configuration so that morphology-controlled nano-size objects can be obtained.[1-5] By using the nanoarchitectonics concept, fullerenes - the well-known ideally zero-dimensional molecular nanocarbon building blocks - can be assembled into a wide variety of nanostructures including one dimensional (1D) fullerene nanowhiskers, two dimensional (2D) fullerene nanosheets, and three dimensional (3D) cubes in the bulk phase or at the liquid-liquid interface.[6-11] These nanostructures result from the supramolecular assembly of fullerene molecules due to π–π stacking interactions.[12] Crystalline fullerene nanomaterials have been extensively used in optoelectronic devices[13-15] and in biomedical research[16-19] and it is a simple matter to control the morphology of the self-assembled fullerene nanostructures.[20] In the liquid-liquid interfacial precipitation (LLIP) method, where crystallization is driven by supersaturation of fullerene in solution at a liquid-liquid interface between typically an alcohol and a solution of fullerene in a good solvent (e.g., toluene), the resulting morphology depends on the synthetic conditions such as

[a] Institute of Polymer Science and Engineering, National Taiwan University, No. 1, Sec. 4, Roosevelt Road, Taipei 10617, Taiwan, R.O.C.. E-mail: shhsu@ntu.edu.tw
[b] International Center for Materials Nanoarchitectonics (WPI-MANA), National Institute for Materials Science (NIMS), 1-1 Namiki, Ibaraki, Tsukuba 305-0044, Japan. E-mail: SHRESTHA.Lokkumar@nims.go.jp
[c] Graduate School of Frontier Science, The University of Tokyo, Kashiwa, Chiba 277-0827, Japan. E-mail: ARIGA.Katsuhiko@nims.go.jp
[†] Electronic Supplementary Information (ESI) available: Figure S1-S29. See DOI: 10.1039/x0xx00000x

composition, solvent type, temperature, antisolvent/solvent volume ratio, etc.[21-23] For example, fullerene C_{60} crystallizes from its solutions in good solvents such as toluene or mesitylene as 1D fullerene nanorods or nanowhiskers upon mixing with alcohols such as methanol (MeOH), ethanol (EtOH), or isopropyl alcohol (IPA).[24,25] On the other hand, 2D fullerene nano/micro sheets are obtained when a solution of fullerene in a solvent mixture composed of carbon tetrachloride (CCl_4) and benzene is mixed with IPA.[26] Similarly, 3D fullerene cubes (FCs) can be assembled from fullerene C_{70} solution in mesitylene upon mixing with tert-butyl alcohol (TBA).[27-29] However, the further structural modification of these micron-sized objects remains a challenging task. The controlled manipulation or organization of micron-sized hollow structures would be useful in certain biological applications where the encapsulation or transport and release of nano or sub-micron-size objects is required.[28]

The applications of fullerene nanostructures in biological fields are very limited due to their hydrophobic nature. For this reason, chemical modification or transformation is required to establish hydrophilic analogues.[30] Afreen et al.[31] used hydrogen peroxide and ultrasound methods to modify pristine fullerenes as hydrophilic fullerenes containing multiple hydroxyl groups (–OH). Wang et al.[32] used sodium hydroxide (NaOH) or tetrabutylammonium hydroxide to functionalize fullerenes with –COOH or –OH functional groups. Similarly, Sun et al.[33,34] used various organic amines to functionalize fullerene molecules by amination reactions. These modifications occur at the molecular level to produce water soluble functional fullerene molecules.[35-37] However, these functional water soluble fullerenes have not been observed to self-assemble to form hollow monodisperse nanostructures.

In this contribution, we report a simple and scalable strategy for the structural modification of self-assembled fullerene crystals, which leads to the formation of hollow and hierarchical fullerene nanostructures, which are different from the previously reported fullerenes assemblies.[38-40] These post-assembled nanostructures have excellent water dispersibility due to surface functionalization with ethylene diamine (EDA). Our method is based on the post-assembly dimension-dependent face-selective etching of fullerene crystals (Scheme 1). Fullerene C_{60} nanorods (FNR), fullerene C_{60} nanosheets (FNS) and fullerene C_{70} cubes (FC) prepared by using the ultrasound assisted liquid-liquid interfacial precipitation (ULLIP) method were mixed with EDA and a mild bath sonication was applied. For 1D FNRs, EDA selectively etches at the both ends of the FNRs resulting in the formation of hollow tubular structures. For 2D FNSs, etching occurred at the upper and lower surfaces of the sheets with only partial etching at their edges. For 3D FCs, etching was rather isotropic and yielded objects with a gyroid-like morphology. These chemically etched fullerene nanostructures showed excellent sensing performance selective for acid vapors (formic and acetic acid) over aromatic vapors (benzene or toluene) due to EDA surface functionalization. These hollow fullerene nanostructures, which are prepared by a simple and scalable solution process, should be useful in biological, ionic sensing, separation, energy storage and drug carrier applications.

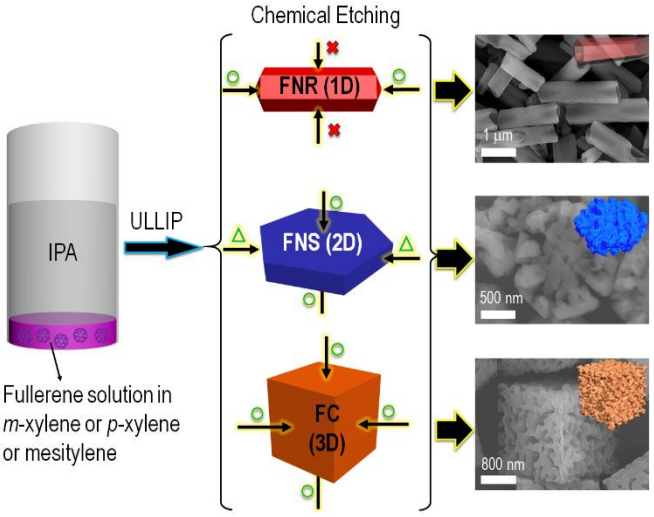

Scheme 1. Schematic representation of the synthesis process of 1D, 2D, and 3D fullerene nanostructures and their face-selective etching with EDA.

Experimental Section

Materials

Pristine fullerene C_{60} and C_{70} powders of 99.5% purity were purchased from MTR Ltd., USA. Isopropyl alcohol (IPA, 99.7%), mesitylene (99.8%) and triethylamine (TEA, 99.0%) were purchased from Nacalai Tesque, Tokyo, Japan. Other solvents *m*-xylene (98.0%), *p*-xylene (98.0%), and ethylene diamine (EDA, 99.0%) were purchased from Wako Pure Chemical Industries, Japan. All the chemicals were used as received.

Synthesis of FNRs, FNSs and FCs

Pristine C_{60} powder was dissolved in *m*-xylene solution by ultrasonication for 1 h. The concentration of C_{60} solution was set at 1.4 mg/mL. FNRs were prepared by using the ultrasonic liquid-liquid interfacial precipitation (ULLIP) method. Fullerene C_{60} solution (1 mL) was placed in a clean and dry 13.5 mL glass bottle placed in a sonication bath and IPA (5 mL) was added rapidly (~ 2 s) into the C_{60} solution under sonication. Sonication was applied for 1 minute then the mixture was removed from the sonication bath and stored undisturbed outside the sonication bath at 25 °C for ~ 5 min. For the preparation of fullerene nanosheets, IPA (5 mL) was added to a fullerene C_{60} solution in *p*-xylene (1 mL: 0.4 mg/mL). For the preparation of fullerene cubes, IPA (2 mL) was added in fullerene C_{70} solution in mesitylene (1 mL: 0.1 mg/mL).

Chemical Etching

Chemical etching was carried out by the addition of EDA solution after the formation of self-assembled fullerene nanostructures. In a typical chemical etching experiment, EDA solution (4%) was added in the mother solution containing fullerene nanorods (or fullerene nanosheets/fullerene cubes) and sonication was applied for 10 min in a bath sonicator and then incubated at 25 °C for different period of times (0 to 24 h). The product obtained was isolated by centrifugation (3500 rpm

for 3 min) and washed with IPA three times prior to characterizations. To study the effect of EDA concentration on etching, different concentrations of EDA (4%, 12%, and 20%) solution were added. In order to study the effect of washing with fresh solvent mixtures on the etching efficiency, the mother liquor including EDA was removed by centrifugation and fresh solvents mixtures (IPA (5mL), *m*-xylene (1mL) and EDA (4%)) were added and sonication was applied for 10 min. Finally, the product was isolated by centrifugation and washed with fresh IPA. The estimation of the remaining volume during the etching of nanorods is based on twenty randomly selected STEM images. From STEM image, we have estimated the thickness of the wall on nanorod, etching depth of nanorod in lumen (*h*), length of nanorod (*H*), diameter of nanorod (*R*), and inner diameter of lumen (*r*). Assuming the shape of etched-volume as a cylinder-like object, volume of etching was calculated as

Volume of etching (%) $=100 \times (2 \times \pi \times (r/2)^2 \times h)/ (\pi \times (R/2)^2 \times H)$

Characterizations

The resulting materials (fullerene crystals before and after amination) were dried at 80 °C in a vacuum oven for 24 h. The morphology of fullerene crystals was examined by using scanning electron microscopy (SEM), scanning transmission electron microscopy (STEM) (both using S-4800 Hitachi Co. Ltd. Tokyo Japan) and transmission electron microscopy (TEM, JEM-2100F, Japan). Crystal structure was evaluated by X-ray diffraction (XRD, RINT-Ultima III, Japan). Surface functional groups were identified using attenuated total reflection-Fourier transform infrared spectrophotometry (ATR-FTIR, Nexus 670, Japan) spectroscopy. Raman scattering spectra were recorded on a Jobin-Yvon T64000 Raman spectrometer with laser wavelength of 514.5 nm at 0.01 mW power. X-ray photoelectron spectroscopy (XPS) measurements were performed on a Theta Probe spectrometer (Thermo Electron Co. Germany) using monochromatic Al-Kα radiation (photon energy 15 KeV). Core level XPS C1s, O1s and N1s were recorded in 0.05 eV steps. A built-in electron flood gun was used during the measurements to avoid sample charging. The UV-vis spectra of FNR, FNS, and FC before and after EDA treatment were collected using a V-670 spectrophotometer (Jasco, Japan) after dispersing them in IPA.

Quartz Crystal Microbalance (QCM)

Vapor sensing performances of the fullerene crystals before and after chemical etching were studied using a quartz crystal microbalance (QCM). A resonance frequency of 9 MHz (AT-cut) was used and the frequency variations recorded for a Au-resonator coated with the respective materials (QCM electrode) during adsorption and desorption of guest vapors. FNR-EDA crystal-modified QCM sensor electrode was prepared as follows: FNR-EDA (0.5 mg) was dispersed in IPA (1 mL) and vortex shaken for 30 s. An aliquot of the resulting suspension (2 μL) was then dropcast onto the QCM electrode (Au-resonator) followed by drying at 80 °C in vacuum for 12 h. FNS-EDA and FC-EDA electrodes were also prepared following a similar method. Resulting QCM electrodes were individually analyzed by setting in the QCM instrument compartment followed by their exposure to solvent vapors (10 mL in an open container) at 25 °C in a sealed chamber (the atmosphere is saturated with the respective solvent vapors). The electrode was exposed to air when the frequency change reached equilibrium in order to desorb any adsorbed materials. For repeatability tests of the QCM electrode, time dependent frequency shift (Δf) was recorded during alternating exposure and desorption of the solvent vapors.

Results and discussion

Ultrasonic-assisted liquid-liquid interfacial precipitation (ULLIP) method[25,27] was used to fabricate fullerene C_{60} nanorods (FNRs), fullerene C_{60} nanosheets (FNSs) and fullerene C_{70} cubes (FCs) at 25 °C. For the fabrication of FNRs, isopropyl alcohol (IPA) and *m*-xylene were respectively used as poor solvent (antisolvent) and good solvent (solvent) for fullerene C_{60}. For FNSs, *p*-xylene was used as a solvent for fullerene C_{60} with IPA as an antisolvent. Similarly, FCs were produced using respectively IPA and mesitylene as antisolvent and solvent for fullerene C_{70}. Details of the synthetic methods are given in the Experimental Section.

Scanning electron microscopy (SEM) images (Figure S1) reveal the formation of straight crystalline FNRs with a uniform size distribution. From a histogram of 100 randomly selected rods, the lengths of the FNRs lie in the 2–3 μm range (Figure S2a) with diameters in the range 500 – 900 nm (Figure S2b). SEM observations reveal that individual FNRs possess highly uniform diameters along the long axis with a small aspect ratio (length/diameter) ca. ~3.6. SEM observation of a single FNR further reveals that FNRs are faceted crystals with the slightly pointed tips (Figure 1a and Figure S1). Scanning transmission electron microscopy (STEM) images (Figure S3) confirm that they are solid. Figure S4 shows SEM images of crystalline 2D FNSs, whose dimensions are found in the range 1.0 - 3 μm (Figure S5). STEM images (Figure S6) also indicate that sheets are solid lacking void spaces. Homogeneous 3D crystalline FCs (Figure S7) are formed with narrow size distributions (Figure S8). FCs have clean surfaces with sharp edges and STEM again reveals that FCs are solid objects with no internal voids (Figure S9).

For chemical etching in solution, these crystalline fullerene nanomaterials; FNRs, FNSs, and FCs were treated with EDA and sonicated for 10 min in a sonication bath then incubated at 25 °C. Interestingly, chemical etching is face-selective and depends on the dimensions of the nanostructures. EDA selectively etches at the ends of the 1D nanorods resulting in the formation of hollow tubular structures (Figure 1g, Figure 1j and Figure S10). The lengths and diameters of the tubular structures (denoted as FNR-EDA) obtained after EDA treatment are not changed by etching (Figure S11). SEM observation reveals that the surfaces of FNR-EDA are less smooth than those of FNRs and also that the diameters of individual tubes is not uniform along their length (Figure S12). This indicates that fullerene molecules at the surfaces of FNRs also partially react with EDA.

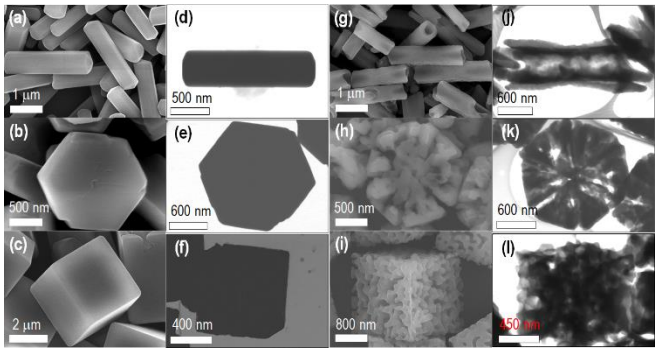

Figure 1. SEM and STEM images taken before and after chemical etching. (a-c) SEM images of FNR (a), FNS (b) and FC (c), (d-f) corresponding STEM images, (g-i) SEM images after chemical etching; FNR-EDA (g), FNS-EDA (h) and FC-EDA (i), and (j-l) corresponding STEM images.

In contrast, for FNS, etching occurs largely at their upper and lower surfaces with only partial etching of their edges (Figure 1h, Figure 1k and Figure S13). Their overall dimensions after etching are unchanged (Figure S14). However, the surface morphology of FNS-EDA differs substantially from the case of FNR-EDA. Macro-channels and macro-sized pores are formed on the surfaces of the FNS (Figure 1h, Figure 1k, Figure S13 and Figure S15). For 3D FC cubes, EDA etching occurs at all faces of the cubes leading to the formation of a gyroid-like morphology (Figure 1i, Figure 1l and Figure S16). Careful observation of SEM images reveals that the cubic shape is maintained and their dimensions are only slightly affected (Figure S17). STEM images further (Figure S18) confirm that etching is highly effective at all faces eventually leading to the formation of a bicontinuous-type channel structure at the cubes' interiors. Transmission electron microscopy (TEM) images confirm the respectively solid then hollow structures of FNRs prior to and following chemical etching (Figure S19a and Figure S19c). Extended lattice fringes of fullerene C_{60} in high resolution transmission electron microscopy (HR-TEM) image confirm the crystalline nature of FNR (Figure S19b) and FNR-EDA (Figure S19b). Similarly, FNS-EDA and FC-EDA also maintain their crystalline form following chemical etching (Figure S19f and Figure S19h).

Structural characterization of the fullerene nanostructures FNR, FNS and FC, prior to and following chemical etching was performed using pXRD, Raman scattering and FTIR spectroscopy. The pXRD pattern of FNRs could be indexed to mixed hexagonal-close pack (*hcp*) and face-centered cubic (*fcc*) crystal structures although pristine C_{60} (pC_{60}) exhibits only *fcc* crystal phase with lattice parameter a = 1.4206 nm with V = 2.867 nm^3 (Figure 2a). Cell dimensions of the *hcp* structure of FNRs were ca. a = 2.3885 nm, c = 1.024 nm (a/c = 2.331), which is similar to the reported *hcp* structures of C_{60} solid solvates.[41,42] The pXRD pattern of FNR-EDA reveals that the diffraction pattern corresponding to the (111) plane of the *fcc* structure present in the FNRs is not present after chemical etching with EDA and FNR-EDA exhibits only the *hcp* crystal structure with cell dimensions ca. a = 2.3849 nm, c = 1.020 nm (a/c = 2.338). The diffraction pattern of FNS shows reflections corresponding to (111), (022), (113), (222), (133) and (024) planes of the *fcc* crystal, which is similar to pristine C_{60} (Figure 2a). Cell dimensions ca. a = 1.4177 nm with V = 2.849 nm^3 are very similar to pristine C_{60}.[8,26] The diffraction

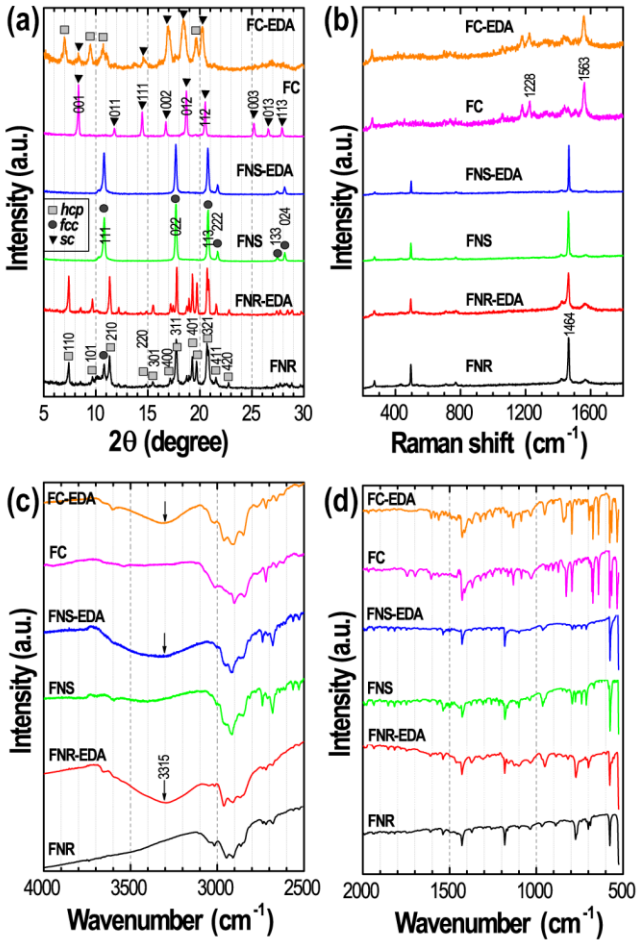

Figure 2. Powder X-ray diffraction (pXRD), Raman scattering and FTIR spectra of fullerene nanostructures before and after chemical etching. (a) pXRD patterns, (b) Raman scattering spectra, (c) high frequency region of FTIR spectra and (d) low frequency region of FTIR spectra of FNR, FNS, FC, FNR-EDA, FNS-EDA and FC-EDA.

pattern is essentially unchanged after chemical etching and the diffraction pattern of FNS-EDA could be indexed to the *fcc* structure with cell dimensions ca. a = 1.4192 nm with V = 2.858 nm^3.

In contrast to pristine C_{70} (pC_{70}) which exhibits an *hcp* structure with lattice parameters a = 1.08 and c = 1.74 nm, the pXRD patterns of FC could be indexed to a simple cubic (*sc*) structure with a cell dimension of a = 1.06 nm and V = 1.194 nm^3 (Figure 2a).[27,28] Following chemical etching the gyroid morphology crystals exhibit mixed *sc* and *hcp* structures with lattice parameters a = 1.05 nm and V = 1.142 nm^3 (for *sc* phase) and a = 1.08 and c = 1.65 nm (for *hcp* phase), respectively.

Raman scattering spectra of FNR-EDA and FNS-EDA are essentially similar to that of FNR, FNS and pristine C_{60} (Figure 2b).[8,26] The pentagonal pinch mode (A_g (2) band) located at 1464 cm^{-1}, which is sensitive to the intermolecular bonding of fullerene C_{60} molecules does not shift after chemical etching indicating that molecular C_{60} dominates in the FNR-EDA and FNS-EDA samples. In the case of fullerene C_{70} cubes, the main peaks are located at 1563 and 1228 cm^{-1} due to the reduction in molecular symmetry (Figure 2b). The main peaks are not affected by chemical etching of FC-EDA indicating that molecular C_{70} dominates the sample. ATR-FTIR spectra of FNR

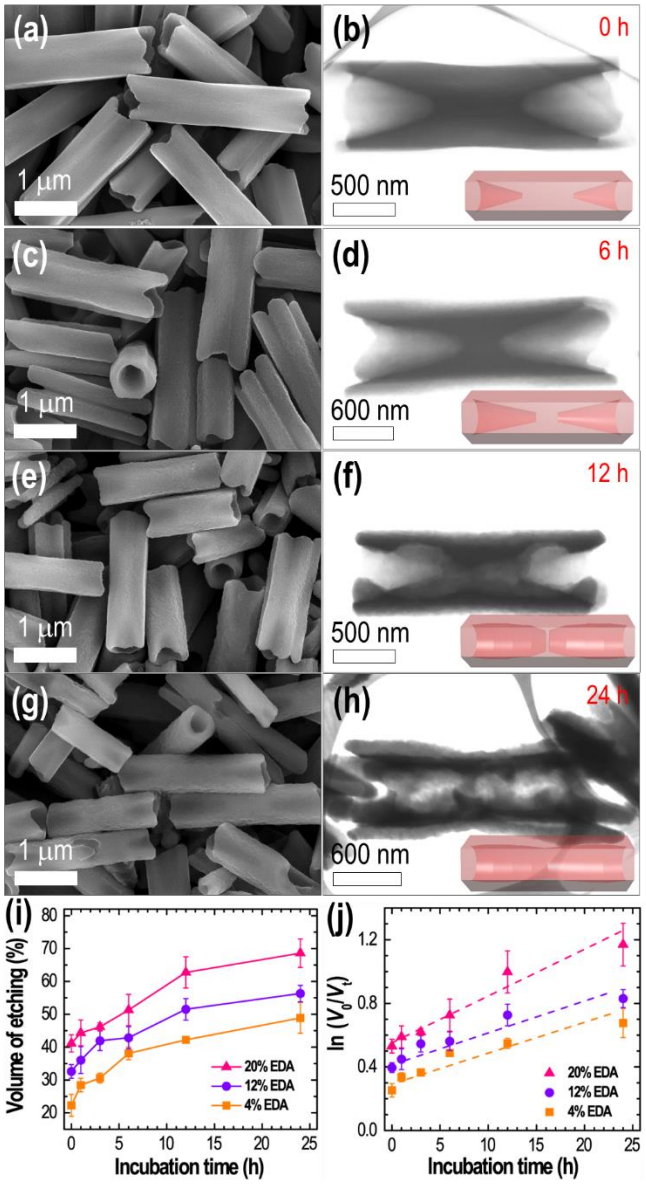

Figure 3. Effect of incubation time on the etching efficiency of EDA on FNRs at 25 °C. SEM (a, c, e and g), STEM (b, d, f and h) images of FNRs at different incubation times (0, 6, 12 and 24 h). (i) Volume of etching vs incubation time at different concentrations of EDA. (j) Kinetics of EDA etching: Natural log plot of V_0/V_t vs incubation time. V_0 is the initial volume of FNR and V_t is the remaining volume of FNRs after etching at different time intervals. Here 0 h stands for the sample immediately following sonication. Insets of panels b, d, f and h show model structures which highlight the extent of etching.

and FNS show four major peaks at 525, 575, 1181, and 1427 cm^{-1}, characteristic of pristine C_{60} indicating that rods and sheets consist largely of molecular C_{60} (Figure 2c,d).[6] Similarly, the FTIR spectrum of FC contains bands characteristic of pristine C_{70}. Minor peaks in the range 3018 to 2900 cm^{-1} can be attributed to C–H stretching vibrations corresponding to the solvent molecules. After chemical etching, all samples (FNR-EDA, FNS-EDA and FC-EDA) exhibit a broad band at 3315 cm^{-1} corresponding to the N–H stretching vibration indicating the presence of EDA-containing species in the samples. Moreover, the intensities of electronic absorption bands are greatly diminished following the treatment of FNR, FNS, and FC with EDA (Figure S20). The colour of solutions of FNR-EDA, FNS-EDA,

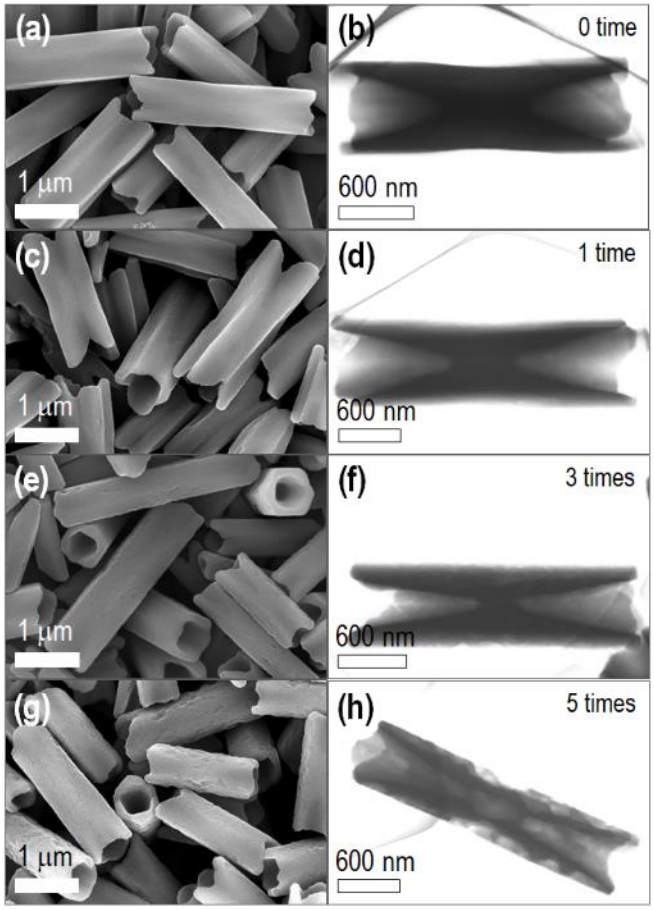

Figure 4. Effect of washing with fresh solvent mixture on the etching efficiency. SEM (a, c, e and g), STEM (b, d, f and h) images of the FNR at different washing (0, 1, 3 and 5 times).

and FC-EDA is yellowish-brown. This indicates that the presence of nitrogen atoms inhibits the Herzberg–Teller vibronic interactions[43] resulting in the attenuation of electronic transitions.

X-ray photoelectron spectroscopy (XPS) survey spectra of pC_{60} and pC_{70}, and FNR, FNS and FC before etching all contain C1s and O1s core level peaks (Figure S21a). The presence of oxygen in the samples is due to aerial oxidation. Relative intensities of the O1s XPS spectra are lower in the self-assembled crystals than in pC_{60} and pC_{70} indicating that aerial oxidation occurs more easily in the pristine forms.[44] Relative intensities of the O1s peaks decreased further and additional N1s core level XPS peaks appeared at around 400 eV (as indicated by arrow) in the chemically etched FNR-EDA, FNA-EDA and FC-EDA samples (Figure S21a). From XPS, nitrogen content was ca. 4.84 atom % (FNR-EDA), 6.1 atom % (FNS-EDA) and 5.3 atom% (FC-EDA). Deconvoluted C1s peaks of pC_{60}, and FNR indicate the presence of C=C (sp^2), C–C (sp^3), O–C=O and C–O bonding states of carbon (Figure S21b). While XPS C1s peaks of FNR-EDA (Figure S21b) reveal that the sample contains the C=C (sp^2), C-N (sp^3) and O–C=O bonding states of carbon. Deconvoluted N1s peaks indicate that nitrogen in the FNR-EDA sample mostly exists in a pyrrolic form (Figure S21c). However, oxidized nitrogen is also present in the FNS-EDA and FC-EDA samples.[45,46]

We have also studied the effect of incubation time on the etching efficiency of EDA in FNR system. For this purpose, EDA [0.24 (4%), 0.7 (12%) and 1.2 mL (20%)] was added into the as prepared FNR [dispersed in the mother liquid of IPA (5 mL) and *m*-xylene (1 mL)] and, after applying sonication for 10 min in a bath sonicator, the mixture was incubated at 25 °C. Etching efficiency was studied by SEM and STEM imaging at different time intervals (0, 6, 12 and 24 h). SEM images (Figure 3a,c,e,g) show that the surface morphology of the FNR-EDA remains essentially unchanged following etching. STEM images (Figure 3b,d,f,h) show that chemical etching in solution is a slow process; the solid cores of the FNRs decrease in thickness with time with etching complete to form a tubular structure being complete after about 24 h of incubation (Figure 3h). For clarity, corresponding model structures are also supplied in the insets of the STEM images. Etching efficiency was also studied at different concentrations of EDA. When EDA concentration is increased from 4 to 20%, the rate of etching of FNR is increased from ~38% to ~51% after 6 h incubation and further increased from ~42% and ~63% after 12 h incubation (Figure 3i).

We have also estimated the initial volume (V_0) and remaining volume of FNRs after etching at different time intervals (V_t) and studied the etching kinetics assuming that the volume is proportional to the amount of the existing reactant. The natural log plot of V_0/V_t versus time follows an approximately linear relationship indicating that etching follows pseudo first-order kinetics (Figure 3j). These results further highlight the time programmed control of the solid core or nano-gap engineering in fullerene crystals.

The effects of washing with fresh solvent mixture on the etching efficiency were also studied in the FNR system. The term 'washing' refers to the replacement of the mother liquor with mixed solvent of the same composition [IPA (5mL), *m*-xylene (1mL) and EDA (20%)]. Washing with fresh solvent mixture also affects the dissolution of the solid cores of the FNRs eventually leading to the formation of the hollow tubular structure after multiple washing (Figure 4).

SEM images (Figure 4a,c,e,g) suggests that the tubular structures have smooth surfaces following washing with the solvent mixtures while STEM images (Figure 4b,d,f,h) clearly reveal the dissolving solid cores and increased overall etching with washing even at the tube outer surfaces. Partially etched FNRs have been converted to tubular hollow structures after 5 cycles of washing with fresh solvent mixture (Figure 4b,h). Also, increasing the EDA concentration in the solvent mixture enhances the etching efficiency (Figure S22). In order to further optimize the EDA etching conditions, we washed the 6 h incubated sample (corresponding to Figure 4c,d) with a solvent mixture containing IPA (5mL), *m*-xylene (1mL) and EDA (20%). In this case, a single washing resulted in the formation of hollow tubular structures (Figure S23 and S24) indicating that both incubation and washing are important for efficient etching. From these results we conclude that the optimum conditions for etching of FNR using EDA is 6 h incubation followed by a single washing with the EDA-solvent mixture.

The chemical etching of self-assembled fullerene crystals is based on the amination reaction between the primary amine,

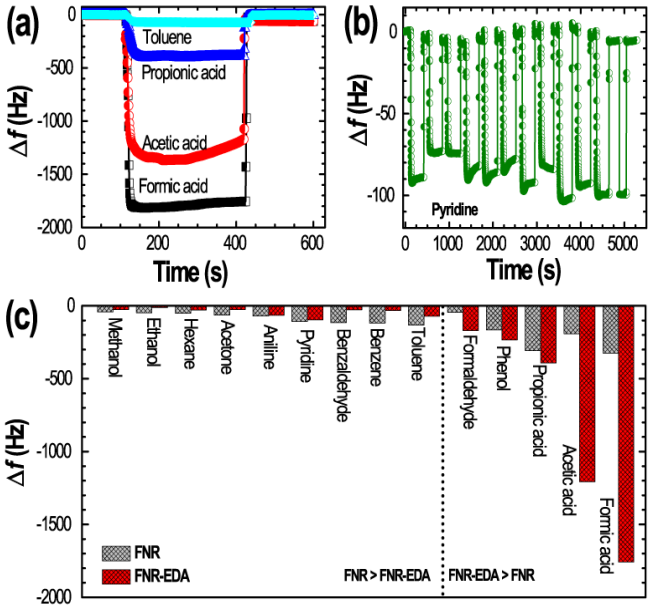

Figure 5. (a) QCM frequency shifts (Δf) upon exposure of FNR-EDA modified QCM electrode to aromatic vapor (toluene) and aliphatic acid vapors (propionic acid, acetic acid and formic acid). (b) Repeatability test up to 12 cycles of FNR-EDA electrode with alternate exposure and removal of pyridine vapor. (c) Summary of sensing performance of FNR prior to and following chemical etching (FNR-EDA).

EDA, and fullerene molecules (Figure S25).[30,33] Amination, a nucleophilic reaction, can take place between amines and fullerenes in a suitable organic solvent medium because of the electron deficiency of C_{60}. Several C_{60} amine derivatives have been reported including aromatic and aliphatic amine derivatives. Moreover, EDA has also been used as a reagent for the modification of usually hydrophobic fullerenes leading to hydrophilic water dispersible products by multiple amination.[30,33] Amination occurs by initial formation of a charge transfer complex between electron rich amine and electron deficient fullerene. Subsequent rearrangement of this state leads to C-N bond formation and the aminated product. Multiple amination of the same molecule can occur by the same mechanisms due to the relative electron deficiency of the products. Mass spectroscopic analysis of the products of etching (measured from solutions of the products) reveals that fullerene C_{60} (m/z = 719.42) remains the major component of the mixtures, as shown in Figure S26a. The etched tubular product contains several additional higher molecular weight species: m/z (a.m.u.) = 777.9 ($C_{60}NH(CH_2)_2NH_2$ $[M - H]^+$), 794.1 ($C_{60}NH(CH_2)_2NH_2(O)$ $[M - H]^+$), 819.7 ($C_{60}NH(CH_2)_2NH_2(O)_2$ $[M - H]^+$), 837.5 ($C_{60}(NH(CH_2)_2NH_2)_2$ $[M - H]^+$), ~860.3 ($C_{60}(NH(CH_2)_2NH_2)_2(O)$) (Figure S26b), and 1501.7 ($(C_{60})_2(NH(CH_2)_2NH_2)$ $[M + 3H]^+$) (Figure S26c). This indicates clearly the reactivity of C_{60} in the etching reaction even in the solid state. To investigate further the amination process, we have also checked the etching efficiency of EDA in the presence of triethylamine (TEA) (Figure S27). Note that TEA is a tertiary amine, functions as a proton inhibitor, and may decrease the proton transfer from EDA to fullerene molecule. This is evident from the weaker etching of FNR in the presence of TEA (TEA:EDA = 10:90) [Figure S27B(b)]. Etching further decreases with increasing TEA and etching did not occur for TEA alone

[Figure S27A(f), S27B(f)]. Contact angle measurements reveal that highly hydrophobic FNRs (contact angle ca. 142°) are transformed to hydrophilic nanotubes (contact angle ca. 43°) by the chemical etching process (Figure S28), which is further confirmed by the greater dispersibility of the aminated product in water (Figure S29).

As mentioned previously, FNR is a solvated solid containing solvent molecules at interstitial sites of the solid phase (~10 wt% *m*-xylene estimated from TGA analysis). If EDA is mixed with FNR after the removal of interstitial solvent, by the heat-treatment of FNR at 220 °C in vacuum for 24 h, selective chemical etching does not occur. Also, pXRD analysis reveals that FNR contains both *hcp* and *fcc* crystal structures. After chemical etching, the *fcc* phase is absent from the FNR-EDA sample. This indicates that interstitial solvent plays a key role in the EDA etching process either by increasing the reactivity of fullerene in solvated regions or by making the corresponding regions less physically stable. This in turn suggests that the end faces of FNR have an *hcp* structure, which is easy to etch. Aminated species that appear at the surfaces of FNR-EDA then originate either from their deposition on *fcc* surface from solution during the etching process or are due to heterogeneous reaction during etching with the *fcc* structure being resisting etching/dissolution.

Different variations in morphology were observed for etching of 2D FNS and 3D FC. In the case of 2D FNS, etching occurred largely at the upper and lower surfaces of the sheets with only partial etching at the edges leading to a porous structure. On the other hand, for 3D FC, etching was isotropic and resulted in the formation of objects with a gyroid-like morphology. pXRD patterns reveal that FNR consists of *hcp* and *fcc* phases. The crystallinity of FNR decreased from 60.7% to 50.2% after etching and the *fcc* phase was eliminated. FNS is of *fcc* structure. The crystallinity of FNS decreased from 51.3% to 14.3% following EDA etching. This could be due to relatively easy etching of the *fcc* phase by EDA molecule as observed for the 1D FNRs. Similarly, crystallinity of FC decreased from 49.5% to 42.1% after etching. Note that FCs exhibit an *sc* structure, while the gyroid-like objects obtained after etching consist of mixed *sc* and *hcp* structures. The emergence of *hcp* structure in the cubes suggests that disassembly and reassembly occur during the reaction. The 3D fullerene cubes have present a uniform structure so that there is an equal likelihood of chemical etching occurring at all faces. Overall, the dimension-dependent face-selective etching of fullerene crystals of different morphology results in the formation of hollow or mesoporous structures, whose structure and hydrophilicity are anticipated to offer new perspectives for interior-integrated nanoarchitectonics and provide useful tools in the biological, drug carrier and molecular sensing.

The etching mechanism for post-assembly fullerene crystals by EDA is complex including co-solvent effects and different crystal forms. The co-solvent used in fullerene nanostructure synthesis influences the morphology of the resulting nanostructures.[47] The EDA solution added into dispersions of self-assembled fullerene crystals affects the solubility of fullerene. C_{60} powder (1.4 mg) can be dissolved rapidly in 1 mL pure *m*-xylene or 1 mL EDA solution after sonication for 10 min. However, in *m*-xylene/IPA (*m*-xylene: 1 mL; IPA: 5 mL) and EDA/IPA (EDA: 1 mL; IPA: 5 mL) mixtures dissolution was less rapid (Figure S30a). The solubility of C_{60} powder in *m*-xylene/IPA and EDA/IPA mixtures are 0.07 and 0.16 mg/mL, respectively. Moreover, the solubilities of post-assembled FNR in the *m*-xylene/IPA and EDA/IPA mixture are 0.03 and 0.11 mg/mL, respectively (Figure S30b); the solubility of FNR is lower than C_{60} powder in the same solvent or solvent mixture. However, while FNR resists dissolution (compared to C_{60} powder), it is still slightly dissolved in EDA/IPA mixture. In this study, EDA solution was added into the post-assembly fullerene dispersion slightly increasing the solubility of fullerenes in the *m*-xylene/IPA mixture. The post-assembly fullerenes have different crystal phases, a feature which increases the resistance to dissolution of the fullerenes. In the case of post-assembly fullerene crystals etched using EDA solution, the order of resistance to dissolution of the crystal phases is *hcp* > *sc* > *fcc* [Figure 2(a)]. The crystal plane on the wall of FNR is the (001) plane of *hcp*. The (001) plane of hcp is densely packed with only small vacancies relative to its other crystal planes. This obstructs effectively the infiltration of EDA (Figure S31). Hence, the EDA etching exhibits face selectivity. The etching order of EDA for FNR is from the ends of FNR.

Fullerene is a π-electron rich nanocarbon material with interesting properties including substantial hydrophobicity and strong van der Waals or π–π interactions derived from its fused π-conjugated structure.[48-51] For this reason, sensing of volatile organic compounds (VOC) using fullerene-based or other nanoporous carbon nanomaterials have received considerable attention.[52-56] Inspired by the aforementioned properties of fullerene together with the mesoporous structure of the aminated products obtained here, we have investigated these self-assembled fullerene nanomaterials for the selective sensing of aromatic solvents and acid vapors using a quartz crystal microbalance (QCM). Figure 5a shows a typical example of time dependent frequency shifts (Δf) for an FNR-EDA modified QCM electrode upon exposure to different solvent vapors (toluene, propionic acid, acetic acid and formic acid).

Frequency shift response is rapid on alternate exposure and removal of the solvent vapors from the QCM sensor compartment with good repeatability (Figure 5a and Figure 5b). Frequency shifts caused by vapor adsorption on the electrode material depends strongly on the type of guest vapors and the electrode material (Figure 5a). In case of the FNR-EDA modified QCM sensor, adsorption of acid vapors such as formic acid (1758 Hz) and acetic acid (1206 Hz) caused large frequency shifts (higher selectivity) compared to vapors of aromatic solvents such as benzene (32 Hz) or toluene (71 Hz) despite the larger saturated vapor pressures of the aromatic vapors. Similar trends in the greater selectivity towards acid vapors was observed using the FNR QCM sensor. However, values of the frequency shifts caused by the adsorption of formic acid (324 Hz) and acetic acid (192 Hz) are small relative to the FNR-EDA sensor. This indicates that acid-base interactions between the acid vapors (formic acid, pK_a = 3.77 and acetic acid, pK_a = 4.75) occur for the FNR-EDA sensor material. It should be noted that

after chemical etching FNR is functionalized with basic amine groups derived from EDA. Further careful observations reveal that FNR is more selective for aromatic solvent vapors than FNR-EDA sensor. Adsorption of aromatic vapors such as benzene and toluene causes large frequency shifts (118 Hz and 131 Hz, respectively) compared to those observed for the FNR-EDA sensor (32 Hz and 71 Hz, respectively). This indicates strong $\pi-\pi$ interactions between host (FNR) and guest molecules (aromatic vapors), which is further confirmed by the poor selectivity of the FNR sensor towards aliphatic hydrocarbon *n*-hexane despite its similar molecular dimensions (Figure 5c and Figure S32a).[27,52] Note that the saturated vapor pressure of hexane (24.78 kPa) is greater than that of benzene (12.68 kPa) and toluene (3.85 kPa). Therefore, the higher observed selectivity towards aromatic vapors is likely due to strong $\pi-\pi$ interactions between aromatic molecules and the sp^2-bonded carbon frameworks of the fullerene molecules. We have also investigated the sensing performance of FNS-EDA and FC-EDA systems. All of the chemically etched fullerene nanostructures follow a similar behavior being more selective towards acids over aromatic vapors. A summary of the sensing performances of FNR-EDA, FNS-EDA and FC-EDA sensors is presented in Figure S32b. Despite the differences in dimensionality of these nanostructures, all the systems studied exhibited selectivity in sensing for the analytes used of formic acid > acetic acid > propionic acid > phenol > formaldehyde > water.

Conclusions

In conclusion, we have successfully demonstrated the post-assembly face-selective chemical etching of the fullerene crystals (fullerene C_{60} nanorods, fullerene C_{60} nanosheet and fullerene C_{70} cubes). Fullerene crystals were produced using the ultrasound assisted liquid-liquid interfacial precipitation method and chemical etching of these products was performed using ethylene diamine. Amination reactions occur because of the high nucleophilicity of ethylene diamine and the relative electron deficiency of fullerene. Etching was found to be face-selective with it occurring anisotropically at the end faces of one-dimensional fullerene nanorods resulting in the formation of hollow structures, fullerene nanotubes. For two-dimensional fullerene nanosheets, etching occurs largely at the upper and lower surfaces of the sheets with only partial etching at the edges. For three dimensional fullerene cubes etching is isotropic occurring at all faces of the cubes resulting in the formation of objects with a gyroid-like morphology. The hollow, porous nanostructures lead to excellent vapor sensing performances for the aminated fullerene nanostructures including selectivity for acid vapors (formic or acetic acids) over aromatic vapors (benzene or toluene). In contrast to costly lithographic techniques often used to prepare nano- and micro-structures, this simple and scalable solution process (for which we coin the term 'beaker lithography') to prepare hydrophilic water dispersible hollow fullerene nanostructures is expected to offer a wide variety of applications including biological, drug carrier and sensing.

Conflicts of interest

There are no conflicts to declare.

Acknowledgements

This work was supported by the Dragon Gate Program, Ministry of Science and Technology, Taiwan, R.O.C. (MOST 106-2911-I-002-571-). This work was partially supported by JSPS KAKENHI Grant Number JP 16H06518 (Coordination Asymmetry) and CREST JST Grant Number JPMJCR1665.

References

1. K. Ariga, M. Matsumoto, T. Mori and L. K. Shrestha, *Beilstein. J. Nanotechnol.*, 2019, **10**, 1559-1587.
2. K. Ariga, X. Jia and L. K. Shrestha, *Mol. Syst. Des. Eng.*, 2019, **4**, 49-64.
3. K. Ariga, M. Nishikawa, T. Mori, J. Takeya, L. K. Shrestha and J. P. Hill, *Sci. Tech. Adv. Mater.*, 2019, **20**, 51-95.
4. J. A. Jackman, N. J. Cho, M. Nishikawa, G. Yoshikawa, T. Mori, L. K. Shrestha and K. Ariga, *Chem. Asian J.*, 2018, **13**, 3366-3377.
5. K. Ariga, Q. Ji, W. Nakanishi, J. P. Hill and M. Aono, *Mater. Horiz.*, 2015, **2**, 406-413.
6. K. Miyazawa, Y. Kuwasaki, A. Obayashi and M. Kuwabara, *J. Mater. Res.*, 2002, **17**, 83-88.
7. L. K. Shrestha, J. P. Hill, T. Tsuruoka, K. Miyazawa and K. Ariga, *Langmuir*, 2013, **29**, 7195-7202.
8. R. G. Shrestha, L. K. Shrestha, A. H. Khan, G. S. Kumar, S. Acharya and K. Ariga, *ACS Appl. Mater. Interfaces*, 2014, **6**, 15597-15603.
9. M. Sathish and K. Miyazawa, *J. Am. Chem. Soc.*, 2007, **129**, 13816-13817.
10. C. Park, E. Yoon, M. Kawano, T. Joo and H. C. Choi, *Angew. Chem. Int. Edit.*, 2010, **49**, 9670-9675.
11. L. K. Shrestha, M. Sathish, J. P. Hill, K. Miyazawa, T. Tsuruoka, N. M. Sanchez-Ballester, I. Honma, Q. Ji and K. Ariga, *J Mater Chem C.*, 2013, **1**, 1174-1181.
12. F. Han, R. Wang, Y. Feng, S. Wang, L. Liu, X. Li, Y. Han and H. Chen, *Nat. Commun.*, 2019, **10**, 1548.
13. D. M. Guldi, B. M. Illescas, C. M. Atienza, M. Wielopolski and N. Martín, *Chem. Soc. Rev.*, 2009, **38**, 1587-1597.
14. J. Li, F. Zhao, T. Wang, M. Nie, J. Li, Z. Wei, L. Jiang and C. Wang, *J. Mater. Chem. A.*, 2017, **5**, 947-951.
15. Y. Ono, T. Akiyama, S. Banya, D. Izumoto, J. Saito, K. Fujita, H. Sakaguchi, A. Suzuki and T. Oku, *RSC Adv.*, 2014, **4**, 34950-34954.
16. S. Goodarzi, T. Da Ros, J. Conde, F. Sefat and M. Mozafari, *Mater. Today*, 2017, **20**, 460-480.
17. P. W. Luo, H. W. Han, C. S. Yang, L. K. Shrestha, K. Ariga and S. h. Hsu, *Adv. Biosyst.*, 2019, **3**, 1800254.
18. F.-Y. Hsieh, L. K. Shrestha, K. Ariga and S.-h. Hsu, *Chem. Commun.*, 2017, **53**, 11024-11027.
19. V. Krishnan, Y. Kasuya, Q. Ji, M. Sathish, L. K. Shrestha, S. Ishihara, K. Minami, H. Morita, T. Yamazaki and N. Hanagata, *ACS Appl. Mater. Interfaces*, 2015, **7**, 15667-15673.
20. L. K. Shrestha, Q. Ji, T. Mori, K. Miyazawa, Y. Yamauchi, J. P. Hill and K. Ariga, *Chem. Asian J.*, 2013, **8**, 1662-1679.

21. C. Park, H. J. Song and H. C. Choi, *Chem. Commun.*, 2009, 4803-4805.
22. J. Kim, C. Park and H. C. Choi, *Chem. Mater.*, 2015, **27**, 2408-2413.
23. J. Kim, C. Park, I. Song, M. Lee, H. Kim and H. C. Choi, *Sci. Rep.*, 2016, **6**, 32205.
24. S. Zheng, N. T. Cuong, S. Okada, T. Xu, W. Shen, X. Lu and K. Tsukagoshi, *Chem. Mater.*, 2018, **30**, 7146-7153.
25. K. Miyazawa, *Sci. Tech. Adv. Mater.*, 2015, **16**, 013502.
26. L. K. Shrestha, Y. Yamauchi, J. P. Hill, K. Miyazawa and K. Ariga, *J. Am. Chem. Soc.*, 2012, **135**, 586-589.
27. P. Bairi, K. Minami, W. Nakanishi, J. P. Hill, K. Ariga and L. K. Shrestha, *ACS nano*, 2016, **10**, 6631-6637.
28. P. Bairi, K. Minami, J. P. Hill, K. Ariga and L. K. Shrestha, *ACS nano*, 2017, **11**, 7790-7796.
29. P. Bairi, S. Maji, J. P. Hill, J. H. Kim, K. Ariga and L. K. Shrestha, *J. Mater. Chem. A.*, 2019, **7**, 12654-12660.
30. I. Rašović, *Mater. Sci. Tech-lond.*, 2017, **33**, 777-794.
31. S. Afreen, K. Kokubo, K. Muthoosamy and S. Manickam, *RSC Adv.*, 2017, **7**, 31930-31939.
32. C. Wang, Y. Bai, H. Li, R. Liao, J. Li, H. Zhang, X. Zhang, S. Zhang, S.-T. Yang and X.-L. Chang, *Part. Fibre Toxicol.*, 2015, **13**, 14.
33. Y. Sun, C. Cao, C. Liu, J. Liu, Y. Zhu, X. Wang and W. Song, *Carbon*, 2017, **125**, 139-145.
34. Y. Sun, C. Cao, P. Huang, S. Yang and W. Song, *RSC Adv.*, 2015, **5**, 86082-86087.
35. T. Xiong and Q. Zhang, *Chem. Soc. Rev.*, 2016, **45**, 3069-3087.
36. A. Ikeda, *J. Incl. Phenom. Macro.*, 2013, **77**, 49-65.
37. W. Si, S. Lu, M. Bao, N. Asao, Y. Yamamoto and T. Jin, *Org. Lett.*, 2013, **16**, 620-623.
38. Z. Tan, A. Masuhara, H. Kasai, H. Nakanishi and H. Oikawa, *Jpn. J. Appl. Phys.*, 2008, **47**, 1426-1428.
39. A. Masuhara, Z. Tan, H. Kasai, H. Nakanishi and H. Oikawa, *Jpn. J. Appl. Phys.*, 2009, **48**, 050206.
40. H.-X. Ji, J.-S. Hu, Q.-X, Tang, W.-G. Song, C.-R, Wang, W.-P. Hu, L.-J. Wan and S.-T. Lee, *J. Phys. Chem. C*, 2007, **111**, 10498-10502.
41. M. Rana, R. Bharathanatha and U. K. Gautam, *Carbon*, 2014, **74**, 44-53.
42. M. Rana, R. B. Reddy, B. B. Rath and U. K. Gautam, *Angew. Chem.*, 2014, **126**, 13741-13745.
43. M. Kanai, K. Porfyrakis, G. A. D. Briggs and T. J. S. Dennis, *Chem. Commun.*, 2004, 210-211.
44. P. Bairi, R. G. Shrestha, J. P. Hill, T. Nishimura, K. Ariga and L. K. Shrestha, *J. Mater. Chem. A.*, 2016, **4**, 13899-13906.
45. D.-W. Kim, O. L. Li and N. Saito, *Phys. Chem. Chem. Phys.*, 2014, **16**, 14905-14911.
46. Z. Yang, M. Xu, Y. Liu, F. He, F. Gao, Y. Su, H. Wei and Y. Zhang, *Nanoscale*, 2014, **6**, 1890-1895.
47. Y. Lei, S. Wang, Z. Lai, X. Yao, Y. Zhao, H. Zhang and H. Chen, *Nanoscale*, 2019, **11**, 8692–8698.
48. H. W. Kroto, A. Allaf and S. Balm, *Chem. Rev.*, 1991, **91**, 1213-1235.
49. C. Park, J. E. Park and H. C. Choi, *Acc. Chem. Res.*, 2014, **47**, 2353-2364.
50. F. Lu, E. A. Neal and T. Nakanishi, *Acc. Chem. Res.*, 2019.
51. S. Das and M. Presselt, *J Mater Chem C.*, 2019, **7**, 6194-6216.
52. N. Furuuchi, R. G. Shrestha, Y. Yamashita, T. Hirao, K. Ariga and L. K. Shrestha, *Sensors*, 2019, **19**, 267.
53. R. Rahimi, S. Kamalinahad and M. Solimannejad, *Mater. Res. Express*, 2018, **5**, 035006.
54. X. Zhang, B. Gao, A. E. Creamer, C. Cao and Y. Li, *J. Hazard. Mater.*, 2017, **338**, 102-123.
55. Y. Kosaki, H. Izawa, S. Ishihara, K. Kawakami, M. Sumita, Y. Tateyama, Q. Ji, V. Krishnan, S. Hishita and Y. Yamauchi, *ACS Appl. Mater. Interfaces*, 2013, **5**, 2930-2934.
56. Q. Ji, I. Honma, S. M. Paek, M. Akada, J. P. Hill, A. Vinu and K. Ariga, *Angew. Chem. Int. Edit.*, 2010, **49**, 9737-9739.